

Geomorphic and geologic controls of geohazards induced by Nepal's 2015 Gorkha earthquake

J. S. Kargel,^{1*†} G. J. Leonard,^{1*} D. H. Shugar,^{2*†} U. K. Haritashya,^{3*†} A. Bevington,⁴ E. J. Fielding,⁵ K. Fujita,⁶ M. Geertsema,⁴ E. S. Miles,⁷ J. Steiner,⁸ E. Anderson,⁹ S. Bajracharya,¹⁰ G. W. Bawden,¹¹ D. F. Breashears,¹² A. Byers,¹³ B. Collins,¹⁴ M. R. Dhital,¹⁵ A. Donnellan,⁵ T. L. Evans,¹⁶ M. L. Geai,¹⁷ M. T. Glasscoe,⁵ D. Green,¹¹ D. R. Gurung,¹⁰ R. Heijnen,⁴ A. Hilborn,¹⁶ K. Hudnut,¹⁸ C. Huyck,¹⁹ W. W. Immerzeel,²⁰ Jiang Liming,²¹ R. Jibson,²² A. Kääh,²³ N. R. Khanal,¹⁰ D. Kirschbaum,²⁴ P. D. A. Kraaijenbrink,²⁰ D. Lamsal,²⁵ Liu Shiyin,²⁶ Lv Mingyang,²⁷ D. McKinney,²⁸ N. K. Nahirnick,¹⁶ Nan Zhuotong,²⁹ S. Ojha,²⁵ J. Olsenholler,³⁰ T. H. Painter,⁵ M. Pleasants,³ Pratima KC,³¹ QI Yuan,²⁶ B. H. Raup,³² D. Regmi,³³ D. R. Rounce,³⁴ A. Sakai,⁶ Shangguan Donghui,²⁶ J. M. Shea,¹⁰ A. B. Shrestha,¹⁰ A. Shukla,³⁵ D. Stumm,¹⁰ M. van der Kooij,³⁶ K. Voss,³⁷ Wang Xin,³⁸ B. Weihs,³⁹ D. Wolfe,⁴⁰ Wu Lizong,²⁷ Yao Xiaojun,⁴¹ M. R. Yoder,⁴² N. Young⁴³

¹Department of Hydrology and Water Resources, University of Arizona, Tucson, AZ, USA. ²School of Interdisciplinary Arts and Sciences, University of Washington Tacoma, Tacoma, WA, USA. ³Department of Geology, University of Dayton, Dayton, OH, USA. ⁴Ministry of Forests, Lands and Natural Resource Operations, Prince George, BC, Canada. ⁵Jet Propulsion Laboratory, California Institute of Technology, Pasadena, CA, USA. ⁶Graduate School of Environmental Studies, Nagoya University, Nagoya, Japan. ⁷Scott Polar Research Institute, University of Cambridge, Cambridge, UK. ⁸Institute of Environmental Engineering, Federal Institute of Technology–ETH, Zurich, Switzerland. ⁹NASA Marshall Space Flight Center, Huntsville, AL, USA. ¹⁰International Centre for Integrated Mountain Development, Kathmandu, Nepal. ¹¹NASA Headquarters, Washington, DC, USA. ¹²GlacierWorks, Marblehead, MA, USA. ¹³The Mountain Institute, Elkins, WV, USA. ¹⁴U.S. Geological Survey, Menlo Park, CA, USA. ¹⁵Central Department of Geology, Tribhuvan University, Kirtipur, Kathmandu, Nepal. ¹⁶Department of Geography, University of Victoria, Victoria, BC, Canada. ¹⁷CVA Engineering, Suresnes, France. ¹⁸Earthquake Science Center, U. S. Geological Survey, Pasadena, CA, USA. ¹⁹ImageCat Inc, Long Beach, CA, USA. ²⁰Faculty of Geosciences, Utrecht University, Utrecht, Netherlands. ²¹State Key Laboratory of Geodesy and Earth's Dynamics, Institute of Geodesy and Geophysics, Chinese Academy of Sciences, Wuhan, Hubei Province, China. ²²U.S. Geological Survey, Golden, CO, USA. ²³Department of Geosciences, University of Oslo, Blindern, Oslo, Norway. ²⁴Hydrological Sciences Laboratory, NASA Goddard Space Flight Center, Greenbelt, MD, USA. ²⁵Graduate School of Environmental Studies, Nagoya University, Nagoya, Japan. ²⁶Cold and Arid Regions of Environmental and Engineering Research Institute, Chinese Academy of Sciences, Lanzhou, China. ²⁷School of Earth Sciences and Engineering, Nanjing University, Nanjing, China. ²⁸Department of Civil, Architectural and Environmental Engineering, University of Texas at Austin, Austin, TX, USA. ²⁹School of Geography Science, Nanjing Normal University, Nanjing, China. ³⁰Department of Geography, Texas A&M University, College Station, TX, USA. ³¹Arizona Remote Sensing Center, School of Natural Resources and the Environment, University of Arizona, Tucson, AZ, USA. ³²National Snow and Ice Data Center, University of Colorado, Boulder, CO, USA. ³³Himalayan Research Center, Kathmandu, Nepal. ³⁴Environmental and Water Resources Engineering, University of Texas at Austin, Austin, TX, USA. ³⁵Wadia Institute of Himalayan Geology, Dehradun, India. ³⁶MacDonald Dettwiler and Associates – GSI, Ottawa, Ontario, Canada. ³⁷Department of Geography, University of California - Santa Barbara, Santa Barbara, CA, USA. ³⁸College of Architecture and Urban Planning, Hunan University of Science and Technology, Xiangtan, China. ³⁹Geography Department, Kansas State University, Manhattan, KS, USA. ⁴⁰GLIMS Steward, Alaska Region, Anchorage, AK, USA. ⁴¹College of Geographical Science and Environment, Northwest Normal University, China. ⁴²Department of Physics, University of California - Davis, Davis, CA, USA. ⁴³Antarctic Climate and Ecosystems Cooperative Research Centre, University of Tasmania, Hobart, TAS, Australia.

*These authors contributed equally to this work.

†Corresponding author. Email: kargel@hwr.arizona.edu (J.S.K.); dshugar@uw.edu (D.H.S.); uharitashya1@udayton.edu (U.K.H.).

The Gorkha earthquake (M 7.8) on 25 April 2015 and later aftershocks struck South Asia, killing ~9,000 and damaging a large region. Supported by a large campaign of responsive satellite data acquisitions over the earthquake disaster zone, our team undertook a satellite image survey of the earthquakes' induced geohazards in Nepal and China and an assessment of the geomorphic, tectonic, and lithologic controls on quake-induced landslides. Timely analysis and communication aided response and recovery and informed decision makers. We mapped 4,312 co-seismic and post-seismic landslides. We also surveyed 491 glacier lakes for earthquake damage, but found only 9 landslide-impacted lakes and no visible satellite evidence of outbursts. Landslide densities correlate with slope, peak ground acceleration, surface downdrop, and specific metamorphic lithologies and large plutonic intrusions.

On 25 April 2015 and over the next several weeks, a major series of displacements occurred ~15 km deep along the buried Main Himalayan Thrust without breaking the surface (1–3). The main shock of the Gorkha earthquake (Magnitude, M 7.8, USGS; epicenter 28.147°N, 84.708°E) was followed by ~257 aftershocks >M 3.0 including 5 ≥M 6.0

between 25 April and 10 June 2015. On 12 May, a M 7.3 aftershock struck ~150 km ENE of the main shock. The largest earthquakes caused a wide swath of casualties and destruction in Nepal and adjacent India, China, and Bangladesh. Some mountain villages were shaken to complete destruction (4), buried by avalanches and landslides, or destroyed

by powerful avalanche and landslide air blasts. The remote locations and blocked roads and rivers meant that ground crews could not immediately access many Himalayan valleys.

We adopted a satellite-based approach to examine the vast damaged region. Satellite imagery was provided by NASA, DigitalGlobe, the Japan Aerospace Exploration Agency (JAXA), MacDonald Dettwiler and Associates (MDA), Planet Labs, Spot Image, and the China National Space Administration, including imagery triggered by the International Charter: Space and Major Disasters (<http://www.disasterscharter.org>). A “Volunteer Group” of analysts from nine nations was organized by the University of Arizona under the auspices of Global Land Ice Measurements from Space (GLIMS) (5) initially to assess priority hazard situations and then to build a landslide inventory (6). The group contributed their input of mapped geohazards to a broad ad hoc NASA-led interagency “Response Team.” We scrutinized optical imagery, ranging from 15 m resolution to <1 m, from Landsats 7 and 8, the Advanced Spaceborne and Thermal Emission and Reflection Radiometer (ASTER) onboard Terra, Advanced Land Imager on EO-1, WorldView-1, -2, and -3, GeoEye-1, Pleiades, and Gaofen-1 (table S1), and utilized radar data from ALOS-2 and RADARSAT-2 and topography from the Shuttle Radar Topography Mission (SRTM). Landslides not detectable at these scales would generally have lesser human consequences than larger landslides.

The Response Team, including the Volunteer Group, undertook one of the broadest and fastest international emergency remote sensing and data analysis campaigns ever led by NASA for any earthquake-affected region (7–9). Parallel, but independent, landslide mapping efforts have been undertaken by a joint British Geological Survey-Durham University group (10) and other groups.

During previous earthquake emergencies in mountainous terrain (e.g., Wenchuan, China; Denali, Alaska), landslides were numerous (9, 11–17), sometimes initiating a process chain of secondary and tertiary geomorphic processes over time-spans ranging from minutes to years after the earthquake (18, 19). Landslide-initiated process chains may involve gains in mobilized mass and destructive power through energy and mass transfer cascades. Many documented or inferred examples exist, including rock/ice fall-generated debris avalanches that transformed into debris flows (20, 21) or caused large impoundment lakes and upstream flooding (22), landslide-generated displacement waves and glacier lake outburst floods (GLOFs) (23, 24), and landslide-dammed lake outbursts (25, 26). As debris, ice, lake and stream water are ingested into an outburst flood, a debris flow or hyper-concentrated slurry flood may result (21). Each geomorphic process in the chain may trigger a subsequent geohazard and extend the damaging reach of the event (27, 28). Process chains involving GLOFs are particularly worrisome.

The Volunteer Group’s work focused on systematic mapping of quake-induced geohazards, understanding the geomorphic, lithologic and tectonic control of their distribution, and the identification of communities and infrastructure that might be affected. We analyzed the distribution and character of the geohazards induced by the Gorkha earthquake in Nepal and Tibet using mainly satellite-based findings, supplemented with media reports, eyewitness photography, helicopter-borne field assessments, and modeling of lake outburst flood processes. This paper considers earthquake-related landslides formed prior to 10 June 2015, when the monsoon arrived in eastern Nepal.

Landslide mapping and assessment

We mapped the distribution of 4,312 earthquake-induced (co-seismic and post-seismic) landslides (Fig. 1). We identified six Areas of Interest (AOIs) that include Annapurna, Manaslu, Ganesh Himal, Langtang, Cho Oyu, and Everest (fig. S1) from west to east. The AOIs together cover 375×155 km, with divisions set along major valleys. Each AOI team had remote sensing and landslide expertise and was assigned an experienced lead analyst.

Multispectral satellite images from many government and commercial sensors (table S1) were made available through a number of portals, including the DigitalGlobe website, the USGS Hazards Data Distribution System (HDDS), and USGS Global Visualization Viewer (GLOVIS). Additionally, NASA provided access to expedited post-earthquake targeted ASTER imagery within the affected region. Not all locations were surveyed repetitively. We compiled a database and detailed descriptions of each AOI (29).

The highest densities of earthquake-related landslides are distributed in a broad swath between the two largest shocks, where many aftershocks also occurred. Clusters of landslides also exist outside of this zone (Fig. 1). The high landslide densities also lie between three >M7.0 earthquakes that occurred on 26 August 1833, 25 April 2015 and 12 May 2015, thus highlighting the possible long-term effects of historic quakes. However, we assessed the landslide occurrences only within the context of the Gorkha earthquake and aftershocks and the terrain characteristics, broadly organized according to (i) surface slopes and the earthquakes’ seismic peak ground accelerations (PGAs), (ii) broad-field deformation due to the earthquakes, and (iii) the distribution of underlying landcover, lithology and tectonic structure.

Among the shaking parameters, PGA is just one factor that may control whether landslides occur in response to an earthquake. The specific frequency content, shake duration, PGA direction, and recurrent shocks also may be important (30). Furthermore, the landslides caused by the Gorkha earthquake and aftershocks appear to be far fewer than expected when compared to other mountainous regions with similar magnitude earthquakes (31, 32). This might be due to the lack of surface ruptures induced by the earthquakes

and the concentration of deformation along the subsurface thrust fault at 10-15 km depth (2).

Landslide distribution: Control by shaking and slope

The locations of the Gorkha earthquake-induced landslides are plotted with landscape physiography and the epicenters of the six largest shocks (Fig. 1A), PGA (Fig. 1B), reported deaths (Fig. 1C), and slope (Fig. 1D). We also map the smoothed landslide density distribution (Fig. 1E), and computed and mapped the susceptibilities of the landscape to earthquake-induced mass movements of ice, snow, or rock (Fig. 2). The computed susceptibilities depend on the product of the sine of slope (33) and the PGA (from the USGS ShakeMap PGA) (Fig. 1B).

Integration of slope and shaking (represented by PGA) within the susceptibility index partly accounts for where landslides occurred (Fig. 2), especially where collapse of high-elevation snow and ice may have been involved (Fig. 2, B and C). The landslide distribution shows the strongest associations with slopes $>30^\circ$ (Fig. 1C and fig. S2A), PGA $>0.32 g$ (Fig. 2A and fig. S2B), and shake-induced landslide susceptibility index $>0.16 g$ (Fig. 2A). We infer that many of these landslides probably would not have occurred anytime soon without earthquake shaking. The control of landslide occurrences by the steep Himalayan slopes and seismic shaking is unsurprising and similar to other well-documented earthquakes (34). However, landslide susceptibilities differ from quake to quake. These new results detail the relationships of this Himalayan earthquake to seismic and geologic/terrain parameters. As PGA attains several tenths of g , entire mountainsides can collapse as shake-induced coseismic failures are not restricted to materials and terrains that were already poised near failure. Whereas landsliding on steep, strongly shaken slopes is easily understood, the tail of the landslide distribution to low shaking values, to low slopes, and low (but nonzero) shaking-induced landslide susceptibilities (fig. S2) requires further explanation.

Under any of the following conditions, low seismic PGAs at a few percent of g may cause failures that lead to a landslide or avalanche if the materials are already near failure:

(i) Granular materials may accumulate near the angle of repose, making them susceptible to coseismic failure due to an acceleration that would increase shear stress along incipient planes of failure or related to rapid coseismic vibration-induced creep (35).

(ii) Seismic vibrations may cause liquefaction of water-saturated sediment, disturbances to the local hydrology, and coseismic or postseismic flow or rotational slumping (36).

(iii) At the beds of polythermal glaciers, the frictional resisting force may be carried by small frozen domains (37). Sharp accelerations may fracture the bed's frozen attachments, thereby suddenly reducing the frictional force and initiating sliding.

(iv) Motion of rock or ice on fracture planes is resisted

by the frictional force at the slip plane (38). Reduction in the normal stress due to downward acceleration, or increase in the downslope driving shear stress due to slip-plane parallel acceleration may initiate coseismically triggered slip on steeply sloping slip planes.

(v) Upward acceleration increases the normal stress and may induce transient pressure melting of basal polythermal ice, thereby reducing the frictional force. The subsequent downward seismic acceleration suddenly relieves the normal stress, such that newly-produced basal meltwater (which might not refreeze) may initiate sliding (39).

The mechanisms outlined above may produce landslides or avalanches at low but nonzero shaking in granular materials occurring on steep slopes, in water-saturated sediments, and on steeply sloping glaciers. The deadly Mount Everest ice/snow avalanches on 25 April 2015 exemplify this point, where shaking was a low $0.09 g$ (table S3). Glacier ice and snow are commonly poised near failure as indicated by Everest's history of ice avalanches off steep slopes, including back-to-back years in which there were a record 16 avalanche deaths in April 2014 (triggered by spring melting) and a new record 22 deaths in April 2015 (earthquake-triggered). Many Himalayan glaciers are substantially avalanche-fed, and snow or ice avalanches may occur upon a slight prompt, whether due to heavy winter or monsoon snowfall, or spring melting, or slight shaking. The Gorkha earthquake struck soon after another season of spring melting began, increasing the vulnerability to shaking of ice and snow in the Everest area. Landslides in the upper Marsyangdi Valley (described below) also experienced relatively weak shaking (0.11 - $0.13 g$), but involved unconsolidated fluvial gravels and lacustrine silts (40).

Seismic reactivation of pre-seismic landslides, or hydrological reactivation of earthquake-triggered landslides, may be common where landsliding already is present. Hydrological reactivations may be caused by precipitation runoff, spring discharge, or erosional undercutting of river banks. Image time series indicate that many mapped landslides, e.g., in the Marsyangdi Valley, happened after the main shock. In general these might be attributable to a host of factors such as aftershocks, failure of earthquake-disturbed hanging glaciers or debuttressed slopes (41, 42), degradation of mountain permafrost and glacier-permafrost interactions (41), extreme precipitation, and stream undercutting of poorly consolidated sediment banks that were already disturbed by the earthquake. These mechanisms involve changes to the supply of ground water or rates of glacial erosion or ice melt, which have at least indirect links to climate change.

Landslide distribution: Control by the broad-field seismic deformation

Another key earthquake phenomenon is the wide-field land surface deformation pattern, which appears to have influenced the distribution of landslides (Fig. 3). The mapped surface deformation was derived from Interfero-

metric Synthetic Aperture Radar (InSAR) (Fig. 3A) (43). While the ALOS-2 InSAR measurement is in the radar line-of-sight, GPS measurements show that the horizontal motion is almost in the along-track direction, so the InSAR displacements in Fig. 3A are almost purely vertical (3). The highest densities of landslides are correlated with the downdropped block, which is on the back-limb of the hanging wall of the thrust and counterintuitively correlates with the higher Himalaya. Within this block, landslide densities increase southward and then abruptly decrease near the tectonic hinge line, which separates the downdropped and upthrown blocks (and also approximates the zone of maximum slip on the fault). RADARSAT-2 data provide the horizontal displacement field over part of the earthquake-affected region and confirm that the largest horizontal displacements (Fig. 3B) are near the hinge line and in the up-lifted block as defined by vertical deformation (Fig. 3A).

We do not fully understand the distinctive concentration of earthquake-induced landslides in the tectonic downdropped block of the Gorkha earthquake. The steep slopes within the downdropped block no doubt contributed to the pattern of landslide densities, but steep slopes are also present in some areas where landslides are few. The net downward acceleration implied by the dropdown possibly caused a momentary reduction in lithostatic stress, hence a reduction of normal stress along inclined planes of weakness. Relief of normal stress could have allowed nonlithostatic shear stress, including lateral seismic acceleration, to initiate motion along landslide failure planes. Because the coefficient of sliding friction is normally less than that of static friction, motion may then continue and drive a landslide. The same mechanism may apply to shaking, and hence, the broad-field deformation may modulate the shaking-induced perturbation of normal stress, again suggesting some integration of multiple causative trigger mechanisms.

The Gorkha earthquake caused fewer landslides than expected based on its magnitude (12, 32), mirroring the unexpected paucity of dwelling destruction (2). The peculiar distribution of the Gorkha earthquake landslides on the downdropped block (Fig. 3) placed them mainly north of the major population centers, reducing the death toll. For strike-slip events such as the 2010 M7.0 Haiti earthquake (44), landslides were not similarly distributed systematically with respect to the fault plane. For comparison, landslides in the 1994 M6.7 Northridge and 2008 M7.9 Wenchuan earthquakes (11, 12, 45) were concentrated on the higher mountainous areas of the upthrown block. Both earthquakes were oblique thrust events, like the Gorkha quake. The Wenchuan earthquake induced far more landslides than the Gorkha earthquake, despite similar steep terrain. These differences might relate to the Gorkha quake's shallow dipping fault and lack of surface rupture (a blind thrust).

The Northridge earthquake was also a blind thrust, and despite being smaller than the Gorkha quake, it produced

11,000 documented landslides (45). Some, mapped by an airborne survey, were smaller than the detection limit in the imagery used for our survey where Digital Globe data were unavailable. The numerous slides caused by the Northridge earthquake may be primarily attributed to uncemented clastic sedimentary compositions dominating the regional lithology, versus more competent high-grade metamorphic and igneous rocks dominating the higher Himalaya. The differing types and densities of vegetation and root binding might also be a factor. In general, differences in earthquake-induced landslide densities can also be related to the number and magnitude of strong high-frequency ground motions, though the paucity of strong-motion recordings in the cases of both the Gorkha and Wenchuan quakes hampers direct comparison.

Landslide distribution: control by lithology and major fault structure

The local clustering indicates additional controls on landslide occurrence. Lithologic variations, sediment thickness, bedding dip direction relative to slope aspect, extent of physical and chemical weathering including extent of bedrock fracturing, and vegetation cover may be important controlling factors. Lithology impacts the occurrence of some landslides. For instance, the Langtang Valley slides involved the failure or ingestion of ice and unconsolidated glacial debris. Another example is the poorly consolidated sediment driving the Marsyangdi Valley landslides.

Fault structures exert indirect control of the clustering of landslides and organization of clusters (Fig. 4). High concentrations of landslides within particular Proterozoic metamorphic units and intrusive complexes and close to the surface traces of several major tectonic features, mainly low-angle thrust faults including the South Tibetan Detachment System (STDS), Main Central Thrust (MCT), Main Boundary Thrust (MBT), and the Main Frontal Thrust (MFT). The latter three faults splay off the subsurface Main Himalayan Thrust, which is thought to have slipped during these earthquakes (1). However, because none of the Gorkha earthquake fault displacements (main shock or aftershocks) are known to have pierced the surface, the association with the thrust faults might indicate underlying lithological control, where the faults juxtapose rocks of differing compositions at the surface. Lithologic properties influenced the topographic character of the landscape and how seismic energy is transmitted, particularly through (i) elastic and brittle/elastic properties of the rock, (ii) chemical weathering and its control of erosion and slope, (iii) fracture development and fault displacement, and (iv) seismic wave interactions with topography and lithological structures. Each factor likely contributes, where lithology is a common denominator. A high density of landslides occurs within the upper Lesser Himalaya near to and east from the epicenter of the primary earthquake. Whereas this cluster's proximity to the largest shock's epicenter is evident, the pattern defined by the cluster is closely correlated with the outcrop of

the upper Lesser Himalaya, which is composed of low- to medium-grade metamorphosed Proterozoic argillic-calcareous (clay and sand) units and also of higher-grade metamorphic Proterozoic rocks. The upper Lesser Himalaya here is bounded on the north by the Main Central Thrust, where the overthrust rocks are dominated by Precambrian gneisses, but only near the thrust contact do the latter underlie many landslides.

Many landslides occur south and west of Kathmandu (Fig. 4) near the southern edge of the Kathmandu Nappe (a thrust sheet of Precambrian/Lower Paleozoic meta-sedimentary rocks as mapped by Stöcklin (46)). In these areas, landslides are especially concentrated where Ordovician granitoids have intruded Proterozoic metasediments, suggesting lithological contrast as a controlling feature. Further, there is a notable absence of landslides south of the MBT-MCT south of Kathmandu.

Proterozoic slate, shale, siltstone, sandstone, graphitic schist (combined as purple in Fig. 4) and gneiss (red in Fig. 4)—all layered rock types—host relatively few landslides. Instead, the vast majority of earthquake-triggered landslides occur in the Proterozoic phyllite, amphibolite, metasandstone, and schist rock sequences of the Lesser and High Himalaya (green and pink in Fig. 4) north of Kathmandu. Notably, these occur on either side of the MCT. The landslide hotspots (Fig. 1E) comprise a small fraction of the area of this widespread rock unit; steep-sided, high-elevation ridgetops generated some of the landslide hotspots. For example, the Langtang Valley landslides largely originated high on the ridges and near the summits in places where glaciers, glacial debris, and bedrock failed. The lithological controls may manifest through rock mechanics and rock weathering and slope.

Topographic effects, along with different rock types' contrasting *s*, *p*, and surface waves impact landsliding through wave scattering, interference, and heterogeneous energy dissipation. During helicopter overflights authors B. Collins and R. Jibson (47) observed pervasive ridgetop shattering through much of the near-epicentral landsliding region. Constructive wave interference and the focusing of seismic energy to shatter ridgetops was observed in the Northridge (48) and 1971 San Fernando (49) earthquakes and modeled for the 2005 I-Lan earthquake in Taiwan (50). Finally, damage related to wave resonance occurred in the Kathmandu Basin during the Gorkha earthquake (2), and similar resonant effects may have occurred elsewhere at damaging frequencies affected by the spatial scales and geometry of various lithologic units. Human-built structures of different sizes and construction, having distinctive resonant vibrational frequencies, were selectively destroyed (2).

Some major river valleys also have high landslide densities, including along the Marsyangdi and Trishuli rivers. In the Marsyangdi Valley, a high landslide density correlates with relatively gently-sloping areas of the valley floor that are covered by poorly consolidated sedimentary deposits.

Langtang mass movements

The earthquake-induced landslides of the Langtang Valley (Fig. 5 and figs. S3 to S6) were exceptional in their tragic results (over 350 killed) and are also among the Gorkha earthquake's best-documented landslides from field- and space-based analysis. Langtang Valley, 70 km north of Kathmandu, is one of Nepal's major trekking regions and hosts benchmark glaciology, hydrology, and meteorology research (51–53). The valley experienced moderate shaking (up to ~0.26 *g* above Langtang village) (Fig. 1B). An analysis of post-event satellite imagery and oblique aerial photographs suggests that co-seismic snow and ice avalanches and rockfalls and their powerful concurrent air blasts contributed to the destruction in Langtang Valley (Fig. 5 and figs. S3 to S6) that killed or left missing at least 350 people (54). Panoramic photos of Langtang taken in 2012 and those taken after the earthquake on 12 May 2015 illustrate the magnitude and destruction of the Langtang events (figs. S3 and S4). Further indicating the vast scale of these events, annotated helicopter-borne photos and satellite imagery taken of the valley (Fig. 5 and figs. S5 and S6) illustrate our interpretation of this disaster-within-a-disaster.

Debris from the initial co-seismic event covered 7.51×10^5 m² at Langtang alone, including a ~1 km stretch of the Langtang River. We did not observe stream impoundment in the days following the earthquake, indicating that melt-water and runoff tunneled rapidly through the icy deposit. Photos (D. Breashears) showed that the deposit contained abundant snow and ice. Brightness temperatures modeled from thermal band 10 of Landsat 8 on 30 April 2015 showed lower landslide surface temperatures (270–280 K) compared to surrounding terrain

(280–300 K). The temperature anomalies, pond formation, and moisture of debris resulted from melting.

The primary coseismic event at Langtang village was a combined ice-snow avalanche that initiated near 7000 m. Subsequently, ice and snow entrained rockfall material and descended a low-gradient part of the glacier down to ~4500 m. The rock-ice mass then became airborne as it fell off a cliff below 4500 m (Fig. 5). After the material reached the riverbed at ~3250 m, it ran up the opposing slope ~200 m (fig. S5). The air blasts propagated farther, 400 m up the mountain (fig. S3). From the impact point on the valley floor, devastation extended ~1 km up- and downvalley. From the 200 m high surge of debris on the opposing slope we estimate a debris speed (*v*) of 63 m s⁻¹ (227 km h⁻¹) following Eq. 1:

$$v = (2gh)^{0.5} \quad (1)$$

where *g* is gravitational acceleration (9.8 m s⁻²), and *h* is the runup. Air blasts leveled what was not buried in Langtang, including some buildings constructed of stone slab. Wind also completely flattened a small forest, suggesting wind speeds comparable to an EF5 tornado (>322 km h⁻¹ wind speed), consistent with freefall drop of the landslide and heavily debris-laden wind over the cliff.

Satellite images provided by Digital Globe (fig. S6) indicate a second large post-mainshock mass movement near Langtang village between 8-10 May 2015. The source of this landslide may have been a rock detachment from the summit ridge of Langtang-Lirung, ~6700 m elevation. The second landslide slightly increased the debris area from $7.51 \times 10^5 \text{ m}^2$ to $7.61 \times 10^5 \text{ m}^2$.

Nearby settlements of Singdum and Mundu (fig. S6) were also damaged by air blasts from the Langtang Valley mass movements. The larger settlement of Kyangjin was also badly damaged by an air blast created by another avalanche that originated from the eastern ridge of Langtang-Lirung. Devastation in the air-blasted zones, as captured in several photos (fig. S3), is indicative of the huge energy involved. The first Langtang landslide mass may be $\sim 3.3 \times 10^9 \text{ kg}$ (area $\sim 750,000 \text{ m}^2$, assumed mean thickness $\geq 2 \text{ m}$, density 2200 kg m^{-3}). With a direct fall of $\sim 1 \text{ km}$ the release of gravitational potential energy was $\geq 3.2 \times 10^{13} \text{ J}$ (7.6-kiloton TNT equivalent). During freefall and impact, the main transfer of energy could only have been to the atmosphere and directly on the surface, the effects of which we sadly observed.

Landslide blockages of rivers: Marsyangdi and Tom rivers (Nepal) and Gyirong Zangbo/Trishuli River (Tibet)

We identified recurrent landslides along the upper Marsyangdi River in the Annapurna region. These are a different type of landslide than those in Langtang Valley. At least twenty mass movements intersected the river in the 10 days following the main shock (Fig. 6). The rapid sequence of similar failures demonstrates that the quakes in some way disturbed the unconsolidated sediments (40) along the river, perhaps by altering the hydrology or opening soft-sediment fractures, which then were exploited by spring seepage/erosion and rotational failures.

The Marsyangdi Valley experienced relatively weak shaking (to $\sim 0.13 \text{ g}$) (Fig. 1B and table S3), which triggered nine small landslides along a 16-km stretch of the upper Marsyangdi River between Humde and Bratang (Fig. 6). The landslides were identified from a WorldView-2 satellite image 27 April 2015, two days after the earthquake, but were not present in a Landsat 8 image four days pre-quake. Thus, we considered them primary effects of the main shock. Some slumps constricted but did not greatly obstruct the river. One landslide (Fig. 6) $\sim 2.2 \text{ km}$ upstream of Lower Pisang village caused a small impoundment (135 m long, $\sim 2 \times 10^3 \text{ m}^2$).

Five more landslides reached the river between 27 April and 2 May 2015, including one $\sim 200 \text{ m}$ wide, which caused a complete blockage $\sim 1.9 \text{ km}$ upstream of Lower Pisang. The impoundment grew to $\sim 550 \text{ m}$ long and 30-40 m wide ($\sim 1.4 \times 10^4 \text{ m}^2$) (Fig. 6). Six new landslides occurred by 4 May, and the lake increased to $\sim 2.5 \times 10^4 \text{ m}^2$ and 1100 m long, the same as measured again on 28 May 2015. Upstream, several smaller impoundments indicated a further hazardous situa-

tion where a dam breach could initiate a succession of lower dam breaches and the inundation of Lower Pisang village.

Ground photographs (Fig. 6B) show a predominantly fine-grained landslide (47), likely composed of fluvial and lacustrine sediments from former dammed lakes (40). The steep headwall, back-tilted trees, and a sharp detachment at the head of the landslide indicate that the slide is a rotational slump, a common failure mode in poorly supported, unconsolidated sediments.

The appearance of eleven post-main-shock landslides and growth of the impoundment lake represent secondary and tertiary effects of the earthquake and indicate that the region is susceptible to long-term slope instability and future landslides.

We observed many other earthquake-induced landslide blockages of rivers. In one case, a 450-m wide landslide blocked the lower Tom River near Ghap, Manaslu Conservation Area, Nepal, creating an impoundment lake that stirred urgent humanitarian concerns. Satellite imagery from 3, 5, 7 and 8 May has allowed monitoring of the dammed lake. Between 3 and 8 May, the lake grew from $\sim 5.7 \times 10^4 \text{ m}^2$ to $\sim 6.6 \times 10^4 \text{ m}^2$. The nearby village of Ghap, located downstream of the confluence of the Tom and Budhi Gandaki rivers, fortunately showed no flood damage by 16 May, indicating that even though the lake was draining through a narrow outlet, the dam erosion was gradual. A satellite image from 8 June and subsequent media coverage shows that most of the lake had drained without severe consequences.

The Gorkha earthquake and its many aftershocks also triggered dozens of landslides into the south-flowing Gyirong River, China (Trishuli River downstream in Nepal). One landslide dammed the river $\sim 1.5 \text{ km}$ south of Chongsecun, a few kilometers north of the Nepalese border, causing development of a $450 \times 50 \text{ m}$ impoundment lake (28.363N, 85.360E, $\sim 2,600 \text{ m}$ asl). The landslide destroyed $\sim 200 \text{ m}$ of the road connecting Chongsecun to the China-Nepal border crossing at Resuo. Boulders and debris were displaced downslope, forming a landslide scar $\sim 700 \text{ m}$ long and a deposit $250 \times 300 \text{ m}$. Several landslides and a landslide-dammed lake also developed south of the Chongsecun slide at or near the Resuo border crossing in Nepal (28.275N, 85.379E, $\sim 1,810 \text{ m}$ asl) and blocked the road near the Resuo bridge. Fortunately, the dam was incised by the river, and with mitigation efforts by engineers there was no further damage. Another landslide on the same river near Resuo was triggered by a rainstorm on 28 April 2015, with the terrain conditioned by the M7.8 Gorkha earthquake. The landslide dammed the Trishuli River and blocked the road from Gyirong County to Resuo Port. These features near Chongsecun and Resuo exemplify the transboundary process chains of some induced hazards. The interruption of cross-border commerce is a major tangible earthquake impact in addition to the damage to infrastructure and the loss of life.

Glacier lakes stability

Many glacial lake outburst floods (GLOFs) have been recorded in the Himalaya since the mid-20th century (55). The lakes' moraine dams, commonly situated at the angle of repose, are fragile and prone to outburst due either to sudden collapse or piping erosion, or to gradual degradation due to climatic warming and thaw. Avalanche and landslide-generated displacement waves in the lake are thought to be a common trigger for moraine dam failure (56). Thus, when the largest earthquakes happened, many experts were concerned that shaking may have weakened or collapsed unconsolidated moraine dams of glacial lakes, or may have triggered large displacement waves and GLOFs.

Fortunately, we identified few earthquake effects on glacier lakes. We examined pre- and post-quake satellite images of 491 lakes (locations drawn mainly from the inventory of Fujita *et al.* (57)). The visibility of 15 lakes in our database was unclear (partially shadowed or poor resolution image) but their downstream drainages showed no signs of GLOFs. Only nine of 491 were physically hit by landslides or avalanches. Of these, ice avalanches may have ejected water from two small ponds near Everest, and debris fell onto the frozen surfaces of other lakes without further effect. No lakes in the current satellite survey produced a GLOF as a result of the earthquake. GLOFs generally do not trigger at modeled PGAs up to 0.57 *g* (Fig. 2D). This unexpected result may relate to seismic wave interactions with the topography, where, for shallow hypocenters, PGAs (i) are reduced on valley floors, and (ii) are rapidly reduced by shielding across mountain ranges caused by wave scattering on the topography and petrologic structure (50, 58).

Furthermore, we closely examined three large moraine-dammed glacial lakes (Thulagi, Rolpa, and Imja) (Fig. 7), which have been extensively surveyed, studied, and monitored due to their GLOF risk (55). At Thulagi Lake in the Manaslu region (just west of the Tom River blockage described above) and Imja Lake in the Everest region, no damage was immediately evident in post-quake satellite imagery. However, a small glacial lake on Lhotse Glacier (south of Everest), drained on 25 May 2015, which resulted in an anomalous rise in stream level (59). Small supraglacial ponds commonly drain suddenly due to ice fracturing or other glacier dynamics, and it is unclear if this event was earthquake-related.

We were especially concerned about Tsho Rolpa, located at the terminus of Trakarding Glacier in the Rolwaling Valley, due to its location near the giant aftershock's (M7.3 on 12 May) epicenter. We found no evidence of damage to Tsho Rolpa's damming moraine from examination of WorldView 1 satellite images taken nine days after the initial earthquake, on 4 May 2015, and the NASA's EO-1 satellite image taken five days after the M7.3 aftershock on 17 May. Post-quake field photographs taken by the USGS on 27 May show that the moraine was intact, and the lake was nearly brim-full (Fig. 8A). Another USGS photograph (Fig. 8B) shows fractures on the moraine dam, but because no ice exists in

this part of the moraine, these tension cracks appear to have been caused by slumping of moraine material toward the lake (1-1.5 m horizontal and ~0.5 m vertical), probably due to an earthquake but not likely to be a problem. The satellite imagery and field photographs do not demonstrate any big new additional concerns about the lake. We would not observe small GLOFs and minor damage to moraines in satellite images due to limitations in resolution. Furthermore, neither satellite and ground nor helicopter-borne inspections can easily detect interior (subsurface) structural damage that make the metastable lakes even more subject to outburst.

Summary and conclusions

Rapid, systematic mapping allowed us to investigate earthquake-induced geohazard processes and provide information to relief and recovery officials on the same timeframe as those operations were occurring. This work thus contributed to effective, timely guidance to in-country authorities responsible for response and recovery. Key findings were relayed through NASA, USGS, and the U.S. Agency for International Development, to Nepal-based experts at ICIMOD (International Centre for Integrated Mountain Development) and DHM (Department of Hydrology and Meteorology, Government of Nepal) and to the Prime Minister of Nepal.

The mapped features document the large geographic extent of the Gorkha earthquake's impact on hazardous Earth surface processes and constrain their geophysical limits and geomorphic, tectonic and lithologic controls. The distribution of induced landslides shows positive associations with slope and shaking intensity. More broadly the highest areal densities of landslides are developed primarily on the downdropped northern tectonic block. This is likely explained by momentary reduction during downward acceleration of the normal stress along planes of weakness. The largest two shocks bracket the landslide distribution, as they are within the displacement field and highest PGAs. Additional controls of landslide distribution are indicated by their clustering within specific bedrock and surficial lithologies including Proterozoic metamorphic rocks and Ordovician granitoids; in proximity to earthquake epicenters; with high PGAs; and perhaps with seismic wave scattering and interferences.

In the remote valleys of the higher Himalaya, the most concentrated losses were directly due to the induced mass movements and air blasts rather than shaking. Seismic wave interactions may have contributed to destruction in Langtang Valley and other locations due to wave focusing and ridgetop shattering but may have reduced direct shaking damage in valley floors and at glacial lakes.

The distribution of Gorkha earthquake-related landslides and the terrain susceptibilities to earthquake-induced mass movements provide a basis from which to predict future patterns of landsliding of earthquake-weakened ice, rock, and unconsolidated sediments, especially as aftershocks,

precipitation, and snowmelt events continue over the next few years. Hydrological processes like frost shattering and rockfalls at high elevations, and riverbank undercutting and rotational slumping in valleys may exploit earthquake-induced damage and trigger more landslides. Conversely, high-magnitude shaking-related landslides, such as ridgetop failures that affected Langtang Valley, may be less common going forward, unless additional strong aftershocks or high-elevation melting affect seismically shattered rocks. However, earthquake-related landsliding may fade below the regional background frequency of landslide activity in the next one to several years.

The Gorkha earthquake caused fewer landslides than comparable earthquakes elsewhere, although some of Nepal's largest mass movements in recent millennia may have been triggered by earthquakes (60). Details of earthquake location relative to geology and topographic relief appear to be crucial in determining the magnitude of earthquake-induced hazards.

Although the Gorkha earthquake's tragic toll on human lives and culture cannot be understated, some fortunate facts are that not a single large GLOF was unleashed and the total number of landslides was far fewer than generated by comparable earthquakes (56). Whether the same will hold for a hypothetical future large Himalayan earthquake is uncertain. However, future earthquakes generated on the shallow Main Himalayan Thrust are not apt to generate many or any GLOFs unless the magnitude is greater than the Gorkha earthquake's or the hypocenter and zone of maximum slip is closer to the lakes, thus circumventing the shielding by Himalayan relief. The potential exists for immense landslides and river blockages, which may pose the greatest mountain hazard.

Materials and methods

We mapped 4,312 landslides from high- and medium-resolution satellite imagery (Landsat 8, WorldView, and others) in the weeks following the M 7.8 main shock. Landslide locations were mapped as points, with attributes including nearest village, dates of imagery used to constrain timing, and whether the mass movement produced or could produce a secondary hazard (e.g., dammed lake). Using a previously published database and the multispectral satellite data, we also assessed damages to glacial lakes. The distribution of landslides was examined in the context of the geology (structure and lithology), the distribution of snow and ice, topographic slopes, and peak ground accelerations modeled for the Gorkha earthquake and its largest aftershock. Seismic and shake intensity data combined with slope were used to model geohazard susceptibility indices. All data, including previously published InSAR-measured ground displacements, were analyzed within a GIS.

REFERENCES AND NOTES

1. R. M. Parameswaran, T. Natarajan, K. Rajendran, C. P. Rajendran, R. Mallick, M. Wood, H. C. Lekhak, Seismotectonics of the April–May 2015 Nepal earthquakes: An assessment based on the aftershock patterns, surface effects and deformational characteristics. *J. Asian Earth Sci.* **111**, 161–174 (2015). doi:10.1016/j.jseaeas.2015.07.030
2. J. Galetzka, D. Melgar, J. F. Genrich, J. Geng, S. Owen, E. O. Lindsey, X. Xu, Y. Bock, J. P. Avouac, L. B. Adhikari, B. N. Upreti, B. Pratt-Sitaula, T. N. Bhattarai, B. P. Sitaula, A. Moore, K. W. Hudnut, W. Szeliga, J. Normandeau, M. Fend, M. Flouzat, L. Bollinger, P. Shrestha, B. Koirala, U. Gautam, M. Bhattarai, R. Gupta, T. Kandel, C. Timsina, S. N. Sapkota, S. Rajaure, N. Maharjan, Slip pulse and resonance of the Kathmandu basin during the 2015 Gorkha earthquake, Nepal. *Science* **349**, 1091–1095 (2015). Medline doi:10.1126/science.aac6383
3. E. O. Lindsey, R. Natsuaki, X. Xu, M. Shimada, M. Hashimoto, D. Melgar, D. T. Sandwell, Line-of-sight displacement from ALOS-2 interferometry: Mw7.8 Gorkha Earthquake and Mw7.3 aftershock. *Geophys. Res. Lett.* **42**, 6655–6661 (2015). doi:10.1002/2015GL065385
4. K. Jaiswal, D. Wald, D. D'Ayala, Developing empirical collapse fragility functions for global building types. *Earthq. Spectra* **27**, 775–795 (2011). doi:10.1193/1.3606398
5. J. S. Kargel, G. J. Leonard, M. P. Bishop, A. Käab, B. H. Raup, *Global Land Ice Measurements from Space*. (Springer-Verlag, Berlin Heidelberg, 2014).
6. E. L. Harp, D. K. Keefer, H. P. Sato, H. Yagi, Landslide inventories: The essential part of seismic landslide hazard analyses. *Eng. Geol.* **122**, 9–21 (2011). doi:10.1016/j.enggeo.2010.06.013
7. J. A. N. van Aardt et al., Geospatial disaster response during the Haiti earthquake: A case study spanning airborne deployment, data collection, transfer, processing, and dissemination. *Photogramm. Eng. Remote Sensing* **77**, 943–952 (2011).
8. G. Cecchine et al., “The U.S. Military Response to the 2010 Haiti Earthquake - Considerations for Army Leaders,” (RAND Corporation, 2013).
9. H. P. Sato, E. L. Harp, Interpretation of earthquake-induced landslides triggered by the 12 May 2008, M7.9 Wenchuan earthquake in the Beichuan area, Sichuan Province, China using satellite imagery and Google Earth. *Landslides* **6**, 153–159 (2009). doi:10.1007/s10346-009-0147-6
10. British Geological Survey, Nepal earthquake response 2015 (available from <http://www.bgs.ac.uk/research/earthHazards/epom/NepalEarthquakeResponse.html>). (2015).
11. R. N. Parker, A. L. Densmore, N. J. Rosser, M. de Michele, Y. Li, R. Huang, S. Whadcoat, D. N. Petley, Mass wasting triggered by the 2008 Wenchuan earthquake is greater than orogenic growth. *Nat. Geosci.* **4**, 449–452 (2011). doi:10.1038/ngeo1154
12. C. Xu, X. Xu, X. Yao, F. Dai, Three (nearly) complete inventories of landslides triggered by the May 12, 2008 Wenchuan Mw 7.9 earthquake of China and their spatial distribution statistical analysis. *Landslides* **11**, 441–461 (2014). doi:10.1007/s10346-013-0404-6
13. R. M. Yuan, Q.-H. Deng, D. Cunningham, C. Xu, X.-W. Xu, C.-P. Chang, Density distribution of landslides triggered by the 2008 Wenchuan earthquake and their relationships to peak ground acceleration. *Bull. Seismol. Soc. Am.* **103**, 2344–2355 (2013). doi:10.1785/0120110233
14. E. L. Harp, R. W. Jibson, R. E. Kayen, D. K. Keefer, B. L. Sherrrod, G. A. Carver, B. D. Collins, R. E. S. Moss, N. Sitar, Landslides and liquefaction triggered by the M 7.9 Denali Fault earthquake of 3 November 2002. *GSA Today* **13**, 4–10 (2003). doi:10.1130/1052-5173(2003)013<0004:LALTB>2.0.CO;2
15. R. W. Jibson, E. L. Harp, W. Schulz, D. K. Keefer, Landslides triggered by the 2002 Denali fault, Alaska, earthquake and the inferred nature of the strong shaking. *Earthq. Spectra* **20**, 669–691 (2004). doi:10.1193/1.1778173
16. D. H. Shugar, J. J. Clague, The sedimentology and geomorphology of rock avalanche deposits on glaciers. *Sedimentology* **58**, 1762–1783 (2011). doi:10.1111/j.1365-3091.2011.01238.x
17. F. C. Dai, C. Xu, X. Yao, L. Xu, X. B. Tu, Q. M. Gong, Spatial distribution of landslides triggered by the 2008 Ms 8.0 Wenchuan earthquake, China. *J. Asian Earth Sci.* **40**, 883–895 (2011). doi:10.1016/j.jseaeas.2010.04.010
18. D. H. Shugar, B. T. Rabus, J. J. Clague, D. M. Capps, The response of Black Rapids Glacier, Alaska, to the Denali earthquake rock avalanches. *J. Geophys. Res.* **117** (F1), F01006 (2012). doi:10.1029/2011JF002011
19. R. N. Parker, G. T. Hancox, D. N. Petley, C. I. Massey, A. L. Densmore, N. J. Rosser, Spatial distributions of earthquake-induced landslides and hillslope

- preconditioning in the northwest South Island, New Zealand. *Earth Surface Dynamics* **3**, 501–525 (2015). doi:10.5194/esurf-3-501-2015
20. S. G. Evans, O. V. Tutubalina, V. N. Drobyshev, S. S. Chernomirets, S. McDougall, D. A. Petrakov, O. Hungr, Catastrophic detachment and high-velocity long-runout flow of Kolka Glacier, Caucasus Mountains, Russia in 2002. *Geomorphology* **105**, 314–321 (2009). doi:10.1016/j.geomorph.2008.10.008
 21. W. Haeblerli, C. Huggel, A. Käab, S. Zraggen-Oswald, A. Polkvoj, I. Galushkin, I. Zotikov, N. Osokin, The Kolka-Karmadon rock/ice slide of 20 September 2002: An extraordinary event of historical dimensions in North Ossetia, Russian Caucasus. *J. Glaciol.* **50**, 533–546 (2004). doi:10.3189/172756504781829710
 22. J. S. Kargel, G. Leonard, R. E. Crippen, K. B. Delaney, S. G. Evans, J. Schneider, Satellite monitoring of Pakistan's rockslide-dammed Lake Gojal. *Eos Trans. AGU* **91**, 394–395 (2010). doi:10.1029/2010EO430002
 23. V. Vilímek, M. L. Zapata, J. Klimes, Z. Patzelt, N. Santillán, Influence of glacial retreat on natural hazards of the Palcacocha Lake area, Peru. *Landslides* **2**, 107–115 (2005). doi:10.1007/s10346-005-0052-6
 24. M. Carey, Living and dying with glaciers: People's historical vulnerability to avalanches and outburst floods in Peru. *Global Planet. Change* **47**, 122–134 (2005). doi:10.1016/j.gloplacha.2004.10.007
 25. S. A. Dunning, N. J. Rosser, D. N. Petley, C. R. Massey, Formation and failure of the Tsatichhu landslide dam, Bhutan. *Landslides* **3**, 107–113 (2006). doi:10.1007/s10346-005-0032-x
 26. J. T. Weidinger, in *Natural and Artificial Rockslide Dams*, S. G. Evans, R. L. Hermanns, A. Strom, G. Scarascia-Mugnozza, Eds. (Springer, Berlin Heidelberg, 2011), pp. 243–277.
 27. M. Geertsema, J. J. Clague, Pipeline routing in landslide-prone terrain. *Innovations* **15**, 17–21 (2011).
 28. K. Hewitt, Disturbance regime landscapes: Mountain drainage systems interrupted by large rockslides. *Prog. Phys. Geogr.* **30**, 365–393 (2006). doi:10.1191/0309133306pp486ra
 29. Materials and methods are available as supplementary materials on Science Online.
 30. Y. Ogata, Statistical models for earthquake occurrences and residual analysis for point processes. *J. Am. Stat. Assoc.* **83**, 9–27 (1988). doi:10.1080/01621459.1988.10478560
 31. D. K. Keefer, Investigating landslides caused by earthquakes - A historical review. *Surv. Geophys.* **23**, 473–510 (2002). doi:10.1023/A:1021274710840
 32. C. Xu, X. Xu, J. B. H. Shyu, Database and spatial distribution of landslides triggered by the Lushan, China Mw 6.6 earthquake of 20 April 2013. *Geomorphology* **248**, 77–92 (2015). doi:10.1016/j.geomorph.2015.07.002
 33. A. Jarvis, H. I. Reuter, A. Nelson, E. Guevara, Hole-filled seamless SRTM data v4 (available at <http://srtm.csi.cgiar.org>). (International Centre for Tropical Agriculture (CIAT), 2008).
 34. P. Meunier, N. Hovius, J. A. Haines, Topographic site effects and the location of earthquake induced landslides. *Earth Planet. Sci. Lett.* **275**, 221–232 (2008). doi:10.1016/j.epsl.2008.07.020
 35. H. T. Chou, C. F. Lee, S. C. Chen, in *Earthquake-Induced Landslides: Proceedings of the International Symposium on Earthquake-Induced Landslides*, K. Ugai, H. Yagi, A. Wakai, Eds. (2013), pp. 45–57.
 36. L. Chen, X. Yuan, Z. Cao, L. Hou, R. Sun, L. Dong, W. Wang, F. Meng, H. Chen, Liquefaction macrophenomena in the great Wenchuan earthquake. *Earthq. Eng. Eng. Vib.* **8**, 219–229 (2009). doi:10.1007/s11803-009-9033-4
 37. P. L. Moore, N. R. Iverson, D. Cohen, Ice flow across a warm-based/cold-based transition at a glacier margin. *Ann. Glaciol.* **50**, 1–8 (2009). doi:10.3189/172756409789624319
 38. H. Blatter, G. K. C. Clarke, J. Colinge, Stress and velocity fields in glaciers: Part II. Sliding and basal stress distribution. *J. Glaciol.* **44**, 457–466 (1998).
 39. N. Bo, J. Persson, in *Sliding on Ice and Snow: Physical Principles and Applications*. (Springer, Berlin, 1998), pp. 391.
 40. J. T. Weidinger, Predesign, failure and displacement mechanisms of large rockslides in the Annapurna Himalayas, Nepal. *Eng. Geol.* **83**, 201–216 (2006). doi:10.1016/j.enggeo.2005.06.032
 41. P. Delincé *et al.*, in *Snow and Ice-Related Hazards, Risks and Disasters*, W. Haeblerli, C. Whiteman, J. F. Shroder, Eds. (Elsevier, Amsterdam, 2015), pp. 521–561.
 42. M. Geertsema, M. Chiarle, in *Treatise on Geomorphology*, J. F. Shroder, M. Stoffel, R. A. Marston, Eds. (Elsevier, Amsterdam, 2013), vol. 7: Mountain and Hillslope Geomorphology, pp. 217–222.
 43. C. Liang, "Interferogram for ALOS2-track 48-swath ScanSARNominal14MHz; Feb 22, 2015 to May 3, 2015," UNAVCO InSAR Product, 10.7283/S2KW2R (2015).
 44. R. W. Jibson, E. L. Harp, "Field reconnaissance report of landslides triggered by the January 12, 2010, Haiti earthquake," (U.S. Geological Survey Open-File Report 2011-1023, Reston, VA, 2011).
 45. E. L. Harp, R. W. Jibson, Landslides triggered by the 1994 Northridge, California earthquake. *Bull. Seismol. Soc. Am.* **86**, S319–S332 (1996).
 46. J. Stöcklin, Geology of Nepal and its regional frame: Thirty-third William Smith Lecture. *J. Geol. Soc. London* **137**, 1–34 (1980). doi:10.1144/gsjgs.137.1.0001
 47. B. D. Collins, R. W. Jibson, "Assessment of existing and potential landslide hazards resulting from the April 25, 2015 Gorkha, Nepal earthquake sequence," (U.S. Geological Survey Open-File Report 2015-1142, Reston, VA, 2015).
 48. J. P. McCalpin, E. W. Hart, "Ridge-top spreading features and relationship to earthquakes, San Gabriel Mountains region, Southern California - Part B: Paleoseismic investigations of ridge-top depressions," *Final Technical Report, Contract 1434-HQ-GR-1026, National Earthquake Hazards Reduction Program* (U.S. Geological Survey, 2002).
 49. R. D. Nason, in *The San Fernando, California, earthquake of February 9, 1971, U.S. Geological Survey Professional Paper 733*. (U.S. Geological Survey, Washington, DC, 1971), pp. 97–98.
 50. S.-J. Lee, D. Komatitsch, B.-S. Huang, J. Tromp, Effects of topography on seismic-wave propagation: An example from northern Taiwan. *Bull. Seismol. Soc. Am.* **99**, 314–325 (2009). doi:10.1785/0120080020
 51. W. W. Immerzeel, L. Petersen, S. Ragettli, F. Pellicciotti, The importance of observed gradients of air temperature and precipitation for modeling runoff from a glacierized watershed in the Nepalese Himalayas. *Water Resour. Res.* **50**, 2212–2226 (2014). doi:10.1002/2013WR014506
 52. K. Fujita, T. Nuimura, Spatially heterogeneous wastage of Himalayan glaciers. *Proc. Natl. Acad. Sci. U.S.A.* **108**, 14011–14014 (2011). [Medline](#) doi:10.1073/pnas.1106242108
 53. S. Ragettli, F. Pellicciotti, W. W. Immerzeel, E. S. Miles, L. Petersen, M. Heynen, J. M. Shea, D. Stumm, S. Joshi, A. Shrestha, Unraveling the hydrology of a Himalayan catchment through integration of high resolution in situ data and remote sensing with an advanced simulation model. *Adv. Water Resour.* **78**, 94–111 (2015). doi:10.1016/j.advwatres.2015.01.013
 54. C. Cadwalladr, Nepal earthquake: the village wiped off the map in a few terrifying seconds. (The Guardian, 2015).
 55. ICIMOD, *Glacial Lakes and Glacial Lake Outburst Floods in Nepal*. (International Centre for Integrated Mountain Development, Kathmandu, Nepal, 2011), pp. 99.
 56. J. J. Clague, S. G. Evans, A review of catastrophic drainage of moraine-dammed lakes in British Columbia. *Quat. Sci. Rev.* **19**, 1763–1783 (2000). doi:10.1016/S0277-3791(00)00090-1
 57. K. Fujita, A. Sakai, S. Takenaka, T. Nuimura, A. B. Surazakov, T. Sawagaki, T. Yamanokuchi, Potential flood volume of Himalayan glacial lakes. *Nat. Hazards Earth Syst. Sci.* **13**, 1827–1839 (2013). doi:10.5194/nhess-13-1827-2013
 58. S. Ma, R. J. Archuleta, M. T. Page, Effects of large-scale topography on ground motions as demonstrated by a study of the San Gabriel Mountains, Los Angeles, California. *Bull. Seismol. Soc. Am.* **97**, 2066–2079 (2007). doi:10.1785/0120070040
 59. A. C. Byers, D. C. McKinney, E. A. Byers, "Post-earthquake assessment: Imja, Tsho Rolpa, and Thulagi glacial lakes in Nepal." (U.S. Agency for International Development, 2015).
 60. W. Schwanghart, A. Bernhardt, A. Stolle, P. Hoelzmann, B. R. Adhikari, C. Andermann, S. Tofelde, S. Merchel, G. Rugel, M. Fort, Oliver Korup, Repeated catastrophic valley infill following medieval earthquakes in the Nepal Himalaya. *Science* (2015). 10.1126/science.aac9865
 61. A. Arendt *et al.*, "Randolph Glacier Inventory – A Dataset of Global Glacier Outlines: Version 4.0," (Global Land Ice Measurements from Space, Boulder, CO, 2014).
 62. U.S. Geological Survey, Earthquake Hazards Program (available from <http://earthquake.usgs.gov>). (2015).
 63. M. R. Dhital, *Geology of the Nepal Himalaya*. Regional Geology Reviews (Springer, 2015).
 64. L. S. Walsh, A. J. Martin, T. P. Ojha, T. Fedenczuk, Correlations of fluvial knickzones with landslide dams, lithologic contacts, and faults in the southwestern Annapurna Range, central Nepalese Himalaya. *J. Geophys. Res.* **117** (F1), F01012 (2012). doi:10.1029/2011JF001984

ACKNOWLEDGMENTS

JSK, GJL, and UKH thank the NASA SERVIR Applied Science Team and NASA Cryosphere Program for support. DHS thanks the Hakai Institute for support. Part of this research was sponsored by the NASA Earth Surface and Interior focus area and performed at the Jet Propulsion Laboratory, California Institute of Technology. We gratefully acknowledge support from several "citizen scientists" who provided key observations and reports from various locations in Nepal: Deep Rai, JB Rai, Nabaraj Sapkota, Mauli Dhan Rai, and Mukhya Gotame, who made on-site inspections and photo documentation of Thulagi (Dona) Lake, Rolpa Lake, Kali Gandaki, and 'Lower Pisang' landslide dammed lake. ASTER data courtesy of NASA/GSFC/METI/Japan Space Systems, the U.S./Japan ASTER Science Team, and GLIMS. We especially laud DigitalGlobe's decision to acquire and make available a vast volume of data for analysis related to Gorkha earthquake response. We thank Cunren Liang for processing the ALOS-2 wide-swath interferogram. Original ALOS-2 data are © 2015 JAXA. This study was partially supported by core funds of ICIMOD contributed by the governments of Afghanistan, Australia, Austria, Bangladesh, Bhutan, China, India, Myanmar, Nepal, Norway, Pakistan, Switzerland, and the United Kingdom. The two chief databases produced by this work are available at ICIMOD (landslides - <http://rds.icimod.org/Home/DataDetail?metadatald=24055>; and glacial lakes - <http://rds.icimod.org/Home/DataDetail?metadatald=24065>).

SUPPLEMENTARY MATERIALS

www.sciencemag.org/cgi/content/full/science.aac8353/DC1

Materials and Methods

Figs. S1 to S6

Tables S1 to S3

20 June 2015; accepted 27 November 2015

Published online 17 December 2015

10.1126/science.aac8353

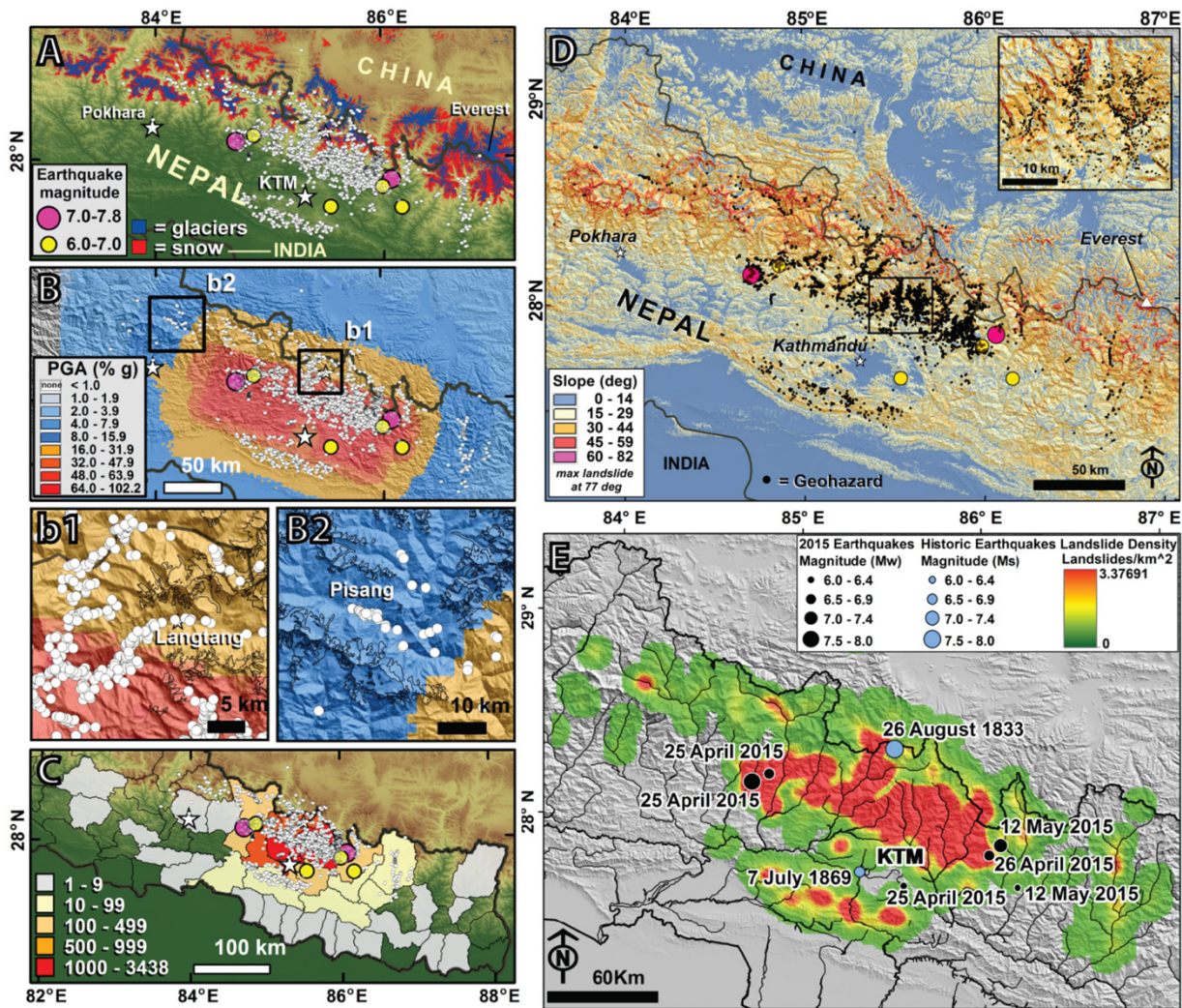


Fig. 1. Location of 4312 earthquake-related geohazards. (A) Distribution of glaciers (blue), late-season snowfields (red), landslides (white dots), and main shock and largest aftershock epicenters. The base topography is from the SRTM 90 m gap-filled DEM (33). Glacier extents are from the Randolph Glacier Inventory (RGI) (61). Snowfields were derived from pre-event Landsat-8 VNIR-SWIR band ratios and topographic masks. (B) Landslides plotted with local peak ground accelerations induced by the main Gorkha shock or >6M aftershocks. PGAs from U.S. Geological Survey's USGS-NEIC ShakeMap (62). Inset panels b1 and b2 are enlarged to show details near Langtang and Pisang. (C) Landslides plotted with reported deaths per Nepal district are from the Government of Nepal, Nepal Disaster Risk Reduction Project. (D) Hazard occurrences (black dots) on calculated slopes. Inset shows detail of hazard-dense region. (E) Smoothed area density (log scale) of earthquake-induced landslides determined using a neighborhood $1/8^\circ \times 1/8^\circ$ search window ($\sim 14 \text{ km} \times 12 \text{ km}$) in relation to major ($\geq M6$) epicenters of historic earthquakes and the Gorkha quakes (62). Densities range between 0.01 and 3.37 landslides/ km^2 . Higher landslide densities occur locally on scales finer than $1/8^\circ$.

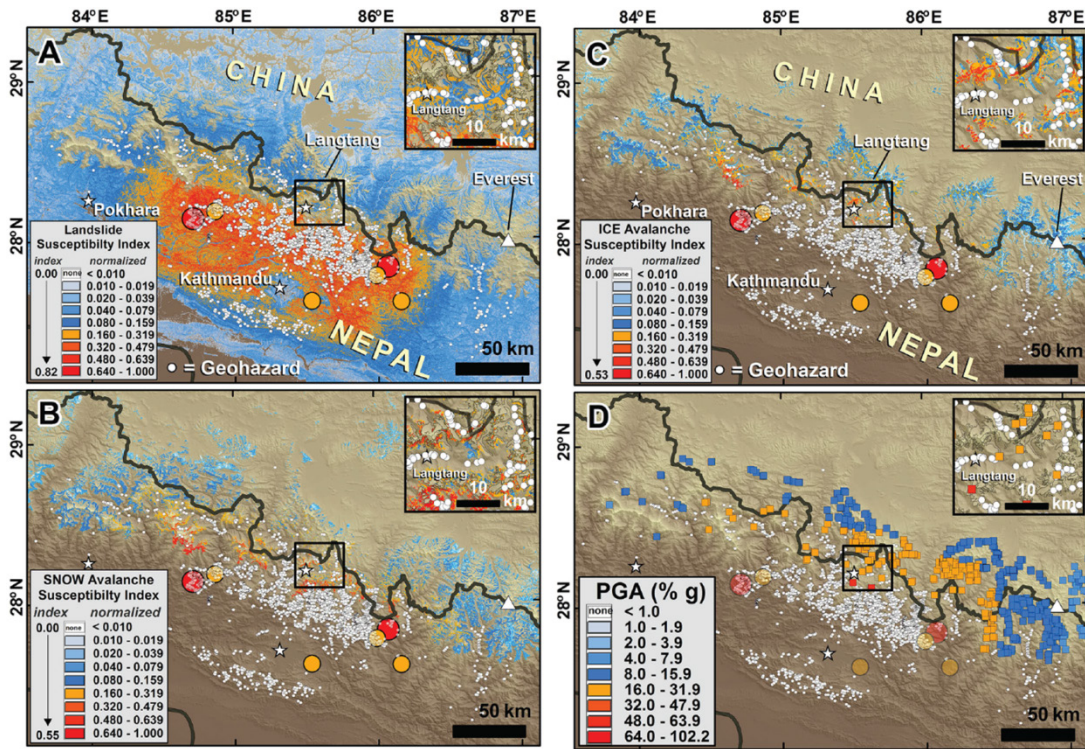


Fig. 2. Debris landslide susceptibility with mapped hazards. (A) Susceptibility in units of acceleration divided by g (9.81 m s^{-2}). **(B)** Snow avalanche susceptibility with mapped hazards. Susceptibility in g . **(C)** Ice avalanche susceptibility with mapped hazards. Susceptibility in g . **(D)** Maximum PGA experienced by 491 glacier lakes. Mapped hazards shown as white dots. Maximum PGA for glacier lakes was $0.57g$. Insets show detail in Langtang Valley.

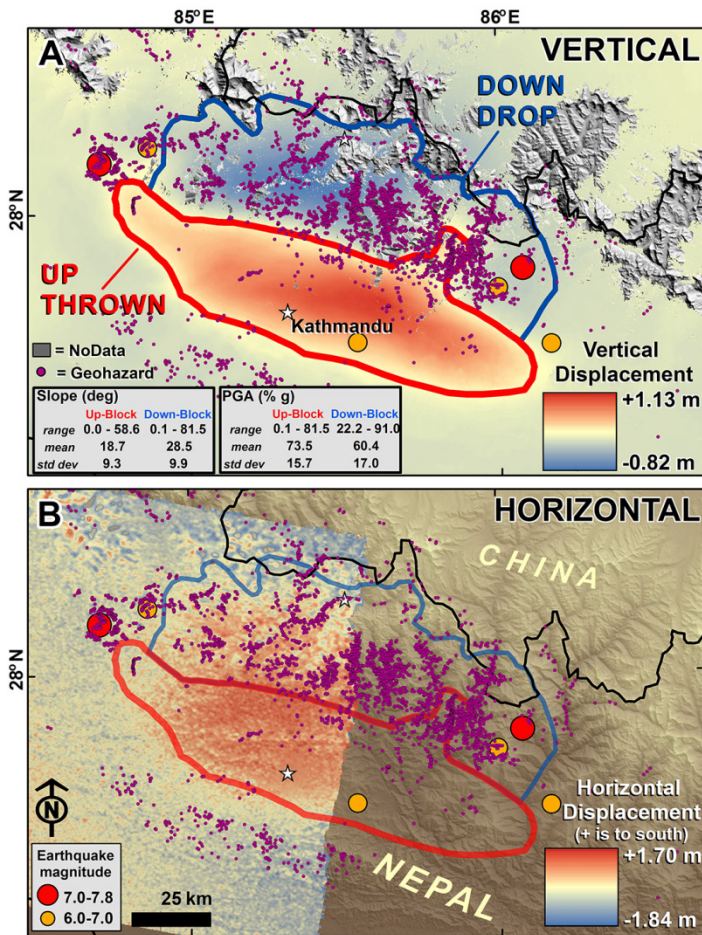


Fig. 3. Landslide distribution relative to the Earth surface deformation field. (A) 4312 landslides (yellow dots) are concentrated mostly north of the hinge line between the downdropped block and uplifted block. Also shown are the epicenters of the main shock and five largest aftershocks. Vertical displacements are from the JAXA ALOS-2 ScanSAR interferogram (21 Feb 21 and 2 May 2015 scenes), which represent almost entirely vertical motion. ALOS-2 interferometry of the Gorkha earthquake and largest aftershock was recently described by Lindsey *et al.* (3). (B) Horizontal motion map based on azimuth shift measurements of the RADARSAT-2 XF acquisitions of 5 April 5 and 29 April 2015. Scale shows motion excluding outliers outside the mean $\pm 3\sigma$. Values are positive for SSW azimuths >100 degrees relative to east (i.e., $>S10W$). Hence, both the upthrown and downdropped blocks shifted southward. Note that the areal coverage for the RADARSAT-2 scene is not identical to that of ALOS-2; areas on the eastern side of the scene have no data.

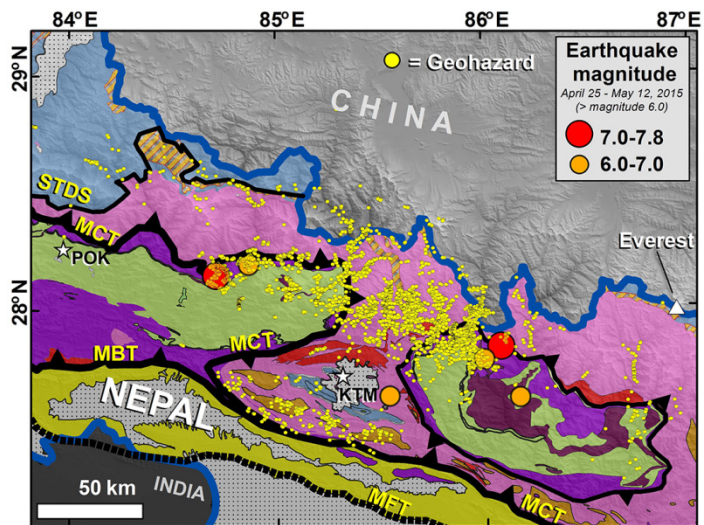
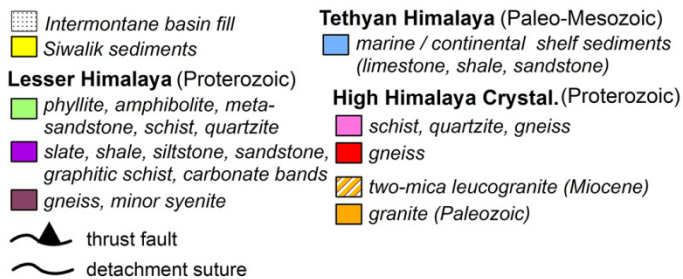


Fig. 4. Landslide occurrence on mapped geologic units. Geology from simplified geologic map by (46, 63)) and major faults (64).



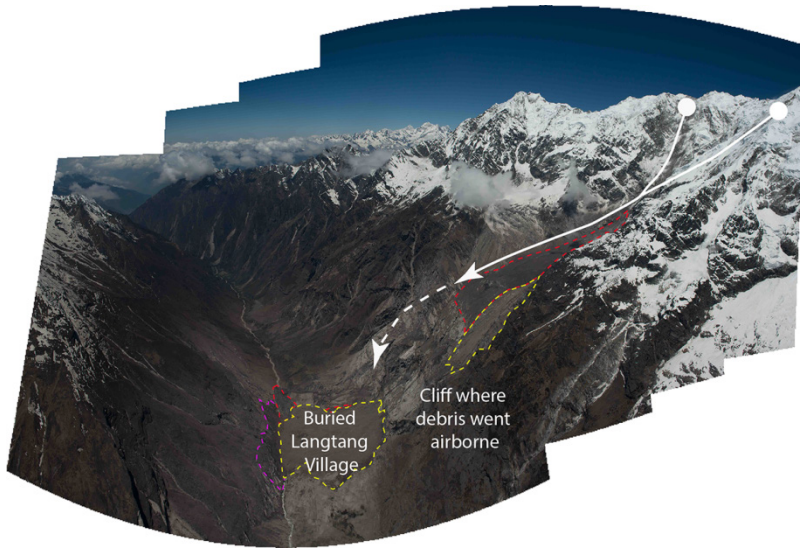


Fig. 5. Langtang's landslide flowpaths. The source areas and flow paths of the two Langtang mass movements (white line, dashed where airborne). Red dashed line indicates the extent of the first slide; yellow dashed line indicates extent of second slide; purple dashed line indicates extent of debris run-up. West facing image. [Stitched panorama from 10 May 2015; photos by D.F. Breashears/GlacierWorks.]

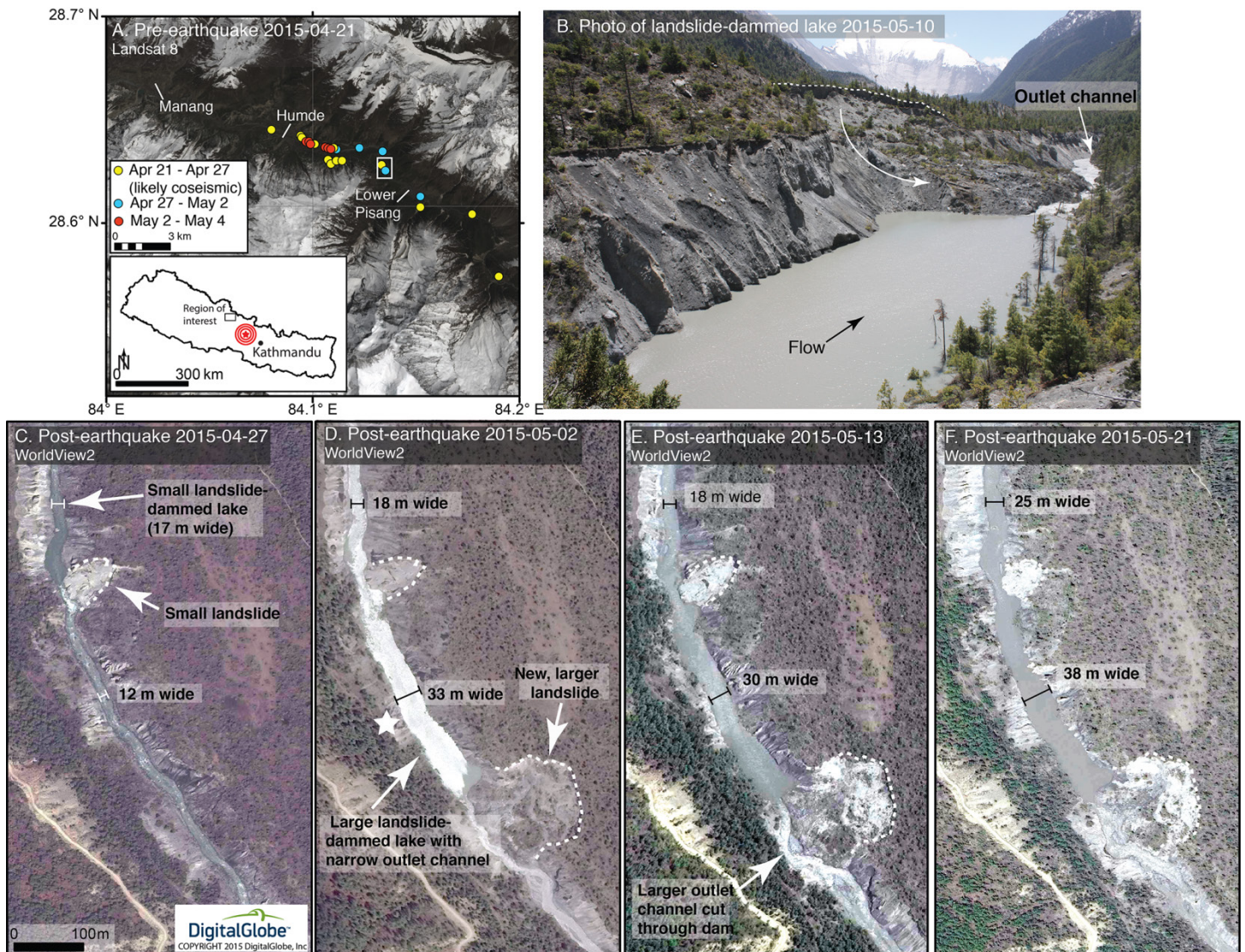


Fig. 6. Landslide-dammed lake on the Marsyangdi River. Map and satellite imagery and ground photographs of landslides and landslide-dammed lakes on upper Marsyangdi River. (A) Map. White box locates (C), (D), (E), and (F). (B) Ground photograph (courtesy Mukhya Gotame, Manang villager) from 10 May 2015, showing the landslide-dammed lake looking south. White dashed line is the head scarp (note steep headwall) and curved arrow shows inferred flow path of the rotational slump. (C, D, E, and F) High-resolution WorldView-2 images of the river, showing delayed occurrence of the large landslide and lake formation. White star in D locates panel B. River widths are given at two locations.

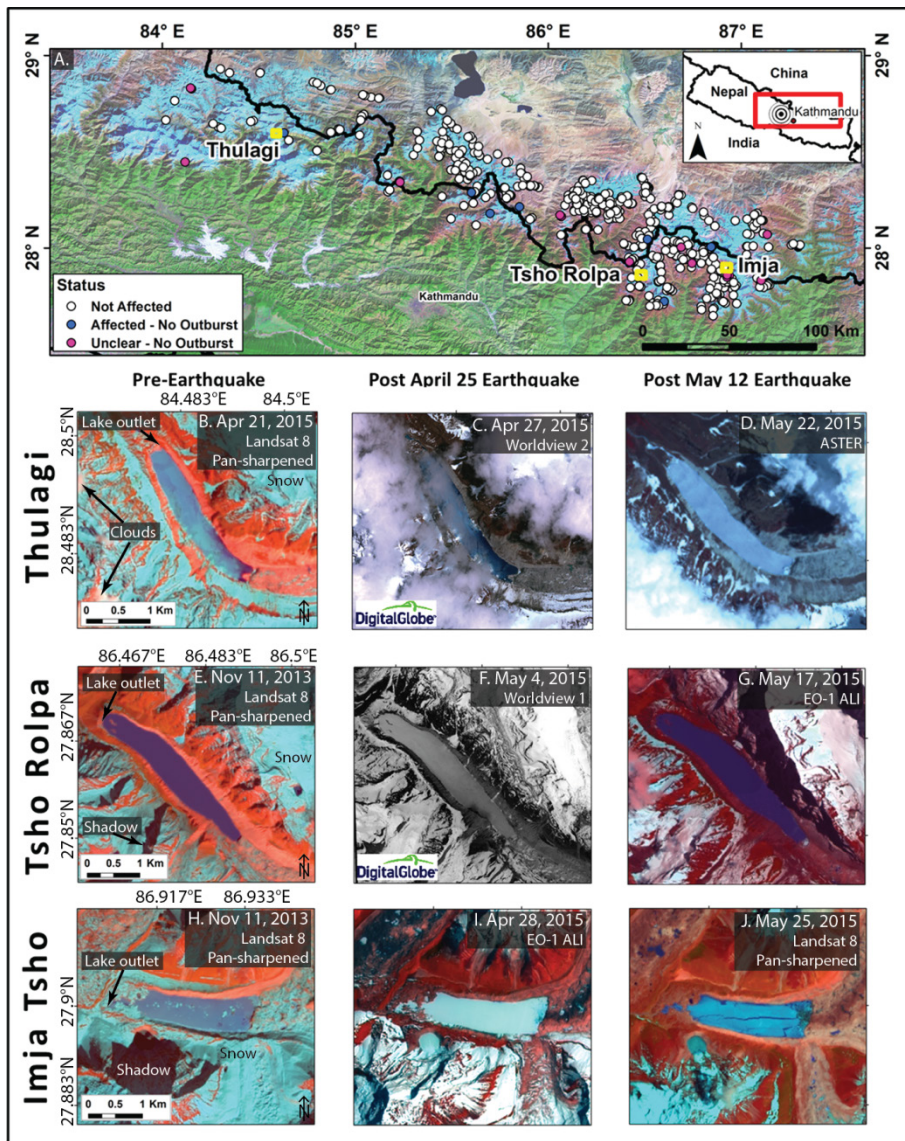


Fig. 7. Lake survey for earthquake damage. (A) (Top) Overview of study area showing location of 491 surveyed lakes. (B to J) pre-earthquake images (right column), post-main shock images (center column) and post-12 May aftershock images (left column) for the largest glacial lakes in Nepal, (B) to (D), Thulagi Lake, (E) to (G) Tsho (Lake) Rolpa, (H) to (J) Imja Tsho. (B) Landsat 8 image of Thulagi Lake, 21 April 2015. (C) Worldview 2 image of Thulagi Lake, 27 April 2015. (D) ASTER image of Thulagi Lake, 22 May 2015. (E) Landsat 8 image of Tsho Rolpa, 11 November 2013. (F) Worldview 1 image of Tsho Rolpa, 4 May 2015. (G) EO-1 ALI image of Tsho Rolpa 17 May 2015. (H) Landsat 8 image of Imja Tsho, 11 November 2013. (I) EO-1 ALI image of Imja Tsho, 28 April 2015. (J) Landsat 8 image of Imja Tsho, 25 May 2015. A large crack developed in the lake ice on Imja Tsho, though such cracks are normal with spring thaw. Landsat 8 scenes are panchromatic band 8 sharpened images (resolution 15 m) using band combinations [7,5,3] (SWIR, NIR, Green). WorldView 2 false color composite scene uses band combination [7, 5, 3] (NIR, Red, Green). WorldView 1 image is the panchromatic band. ASTER image (resolution 15 m) uses bands [3N, 2, 1] (NIR, Red, Green). EO-1 ALI scenes use pan-sharpened band 1 (resolution 10 m) and band combination [8, 6, 4] (SWIR, NIR, Green).

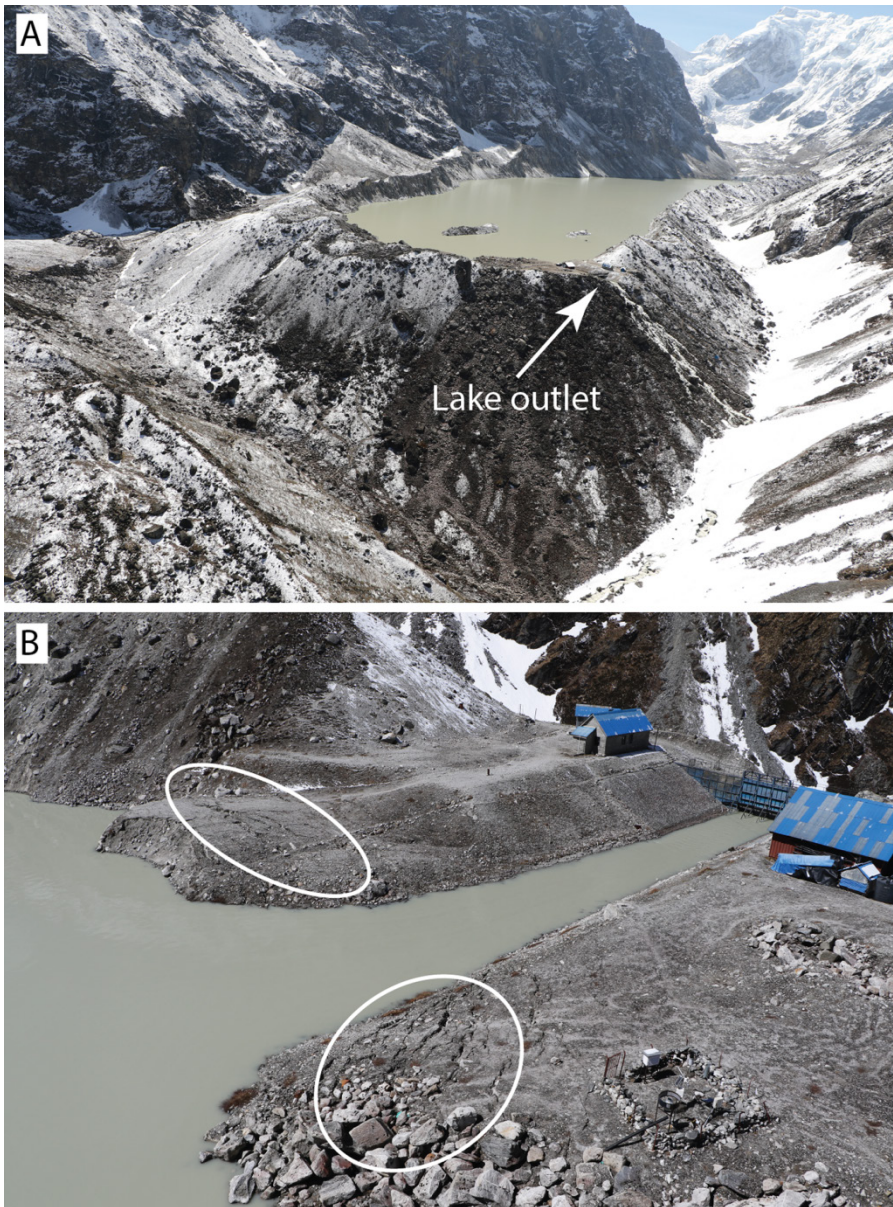


Fig. 8. Field visit identifies light damage at Tsho (lake) Rolpa. (A) Post-earthquake image of Tsho Rolpa appears identical to its appearance shortly before the earthquake. **(B)** Two areas of fractures (outlined in white)—believed formed by the 12 May 2015 aftershock—were observed on the engineered part of the end moraine from a helicopter during an inspection undertaken by the U.S. Geological Survey at Tsho Rolpa. Photos from 27 May by Brian Collins (USGS), courtesy of USAID-OFDA (Office of Foreign Disaster Aid).